Tellus (2002), 54A, 273–287
Printed in UK. All rights reserved

TELLUS
ISSN 0280–6495

Rapid changes of the oceanic circulation in a hierarchy of ocean models

By J. HIRSCHI* and T. F. STOCKER, *Physics Institute, University of Bern, Sidlerstrasse 5, 3012 Bern, Switzerland*

(Manuscript received 21 May 2001; in final form 26 November 2001)

ABSTRACT

The response time of the large-scale oceanic circulation due to freshwater perturbations is investigated with models of different complexity. A three-dimensional ocean general circulation model (OGCM) and a zonally averaged ocean model are employed. In order to distinguish advection and diffusion from fast baroclinic processes (e.g. waves in the OGCM) a color tracer is injected at the same time and location as the freshwater discharges. In spite of the inability of the zonally averaged model to represent wave processes in a realistic way similarities with the OGCM are found for the propagation patterns of density anomalies and of color tracer. In the OGCM as well as in the zonally averaged model, density anomalies propagate faster than anomalies of a passive color tracer in the case of vertical density stratification. The progression of density anomalies leads to changes of the oceanic circulation, and both oceanic models exhibit circulation changes in areas distant from the discharge places long before the passively entrained color tracer has reached these regions. The fact that a zonally averaged model simulates baroclinic processes faster than advection even if internal gravity waves are not represented due to neglected acceleration terms, is clarified with a conceptual box model.

1. Introduction

The adjustment of the oceanic circulation to changed forcing conditions has been the subject of many investigations focusing on the role of the ocean for climate change. A key area of interest is the North Atlantic, where surface water sinks due to strong cooling helping to drive the thermohaline circulation (Dickson and Brown, 1994; Broecker, 1991). Numerous studies are dedicated to the presumed sensitivity of the thermohaline circulation to perturbations such as northern or southern freshwater perturbations, e.g. Mikolajewicz (1998), Manabe and Stouffer (1997), Rahmstorf (1995), Stocker and Wright (1991) or Weijer et al. (1999). Other investigations focus on changes induced by anomalies of the wind field (e.g. Visbeck et al., 1998; McDermott, 1996; Toggweiler and Samuels, 1993) or by an increased frequency of El Niño events due to global warming (Latif et al., 2000; Schmittner et al., 2000). These studies show that changes of the ocean circulation are not confined to their areas of generation but can also be seen in the far-field circulation pattern.

The times needed for anomalies to reach distant areas can vary from decades/centuries for advective/diffusive processes (Pierce et al., 1995) to a few days or weeks for barotropic and baroclinic wave processes (Kawase, 1987). In general, the propagation of an anomaly is due to a superposition of several mechanisms. Depending on the degree of simplification of the employed model these processes are only partly represented. If advection and acceleration terms are retained in

* Corresponding author.
e-mail: jjmh@soc.soton.ac.uk
Present affiliation: School of Ocean and Earth Science, Southampton Oceanography Centre, University of Southampton, United Kingdom.

the momentum equations all three processes occur. However, only wavelengths longer than grid resolution can be resolved, and the phase speed of the simulated waves depends on both grid resolution and grid type (Hsieh et al., 1983). Applying a rigid lid condition at the top of the ocean filters out barotropic gravity waves. Neglecting terms in the momentum equations is a further simplification commonly done in models designed for long time integrations. Maier-Reimer et al. (1993) neglect non-linear terms (advection) for momentum, whereas in the zonally averaged model of Wright and Stocker (1991) both non-linear and acceleration terms are removed from the momentum equations.

For the investigation of timescales covering 10^5–10^6 yr, simplified models are valuable tools due their low computational cost. As an example long time integrations are required, if one is interested in modeling the last glacial period which was characterized by abrupt climatic changes (Stocker, 2000). A problem which is not yet fully understood concerns the connections between the northern and the southern hemispheres during such events (Blunier et al., 1998; Bender et al., 1994). Since the ocean is supposed to play a central role in this problem (Broecker, 1998; Stocker, 1998) it is important to know how interhemispheric coupling is achieved in simplified ocean models and how the related mechanisms and timescales compare with those seen in models with a more complete description of ocean dynamics.

The aim of the present study is to compare the propagation patterns and velocities of density and color tracer anomalies in models of different complexity during and after freshwater perturbations. For this purpose we use a full hierarchy of ocean models: a comprehensive ocean general circulation model (OGCM), a zonally averaged ocean model and a box model. We discuss the similarities and differences between the anomaly propagation patterns generated by these models.

The paper is organized as follows: in Section 2 we briefly describe the oceanic models and their initial circulations; propagation patterns occurring for density anomalies and for a color tracer in the oceanic models are discussed in Section 3; in Section 4 the propagation mechanisms are further illustrated with a conceptual box model; results of the study are summarized in Section 5.

2. Oceanic models and steady states

We use the three-dimensional model of the GFDL in the version of Pacanowski and Griffies (2000) based on the method of Bryan (1969). The ocean geometry consists of one idealized basin of 60° width extending from 75°S to 75°N. Between 65°S and 50°S a channel representing the Antarctic Circumpolar Current (ACC) traverses the basin. The horizontal grid resolution is 2.5° in both longitude and latitude. The ocean depth is 5000 m everywhere except at the eastern and western boundaries of the ACC, where the depth is set to 2500 m. The vertical is divided into 19 levels with thicknesses varying from 30 m at the surface to more than 500 m for the bottom level. The horizontal viscosities and diffusivities are set to 2.5×10^5 m^2 s^{-1} and 2.5×10^3 m^2 s^{-1}. The vertical coefficients are set to 10^{-4} m^2 s^{-1}. Timesteps are set to 1 d for tracers and to 1800 s for momentum during spinup. For freshwater discharge experiments 1800 s are used for both timesteps. We use temporally constant analytical forcing profiles without zonality for wind, temperature and salinity similar to the ones employed in Hirschi et al. (1999).

The two-dimensional model is based on the zonally averaged ocean model of Wright and Stocker (1991). Similar to the OGCM, the ocean is represented by one single basin with the same meridional and zonal extent crossed in the south by the ACC. The horizontal and vertical resolution, the advective and diffusive coefficients as well as the forcing profiles for temperature, salinity and wind are the same as in the GFDL model. The meridional velocity is either calculated according to the closure scheme of Wright and Stocker (1991) or Wright et al. (1995) (WS91 and WVH95, henceforth).

The original closure of WS91 has the form

$$\frac{\Omega}{\varepsilon} v = \frac{1}{\rho_*} \frac{\partial p}{\partial y}, \tag{1}$$

where p is the pressure, ρ_* a reference density and Ω the earth's angular velocity, v is meridional velocity and ε denotes a closure parameter. A constant value of 0.45 is prescribed for ε. WVH95 suggested the following, physically more reasonable closure scheme based on the zonally averaged

vertical component of the vorticity equation:

$$Lv_z = \frac{2g}{f}\left[(\sigma-\sigma_{eq})+\gamma_2\left(\frac{f}{f_{end}}\right)^{\gamma_1} \times(\sigma_{end}-\sigma_{eq})+|f|^{\gamma_1}\int_y^{y_{end}}|f|^{-\gamma_1}\sigma_\zeta\,d\zeta\right] + \frac{r}{f}(Lv_z-Lv_z|eq), \quad (2)$$

where $\sigma=(\rho-\rho_*)/\rho_*$ is the zonal average of the relative density variation and L the zonal basin extent. The Coriolis parameter is denoted by $f=2\Omega\sin y$, and σ_{eq}, σ_{end} are the zonally averaged densities at the equator and at the northern or southern extremities of the ocean basin, respectively. Subscript coordinates indicate partial derivatives in the respective direction where ζ denotes the meridional coordinate. This formulation has three free parameters γ_1, γ_2 and r; they are set to $\gamma_1=1.1$, $\gamma_2=-0.6$ and $r=0$ as in WVH95.

In addition to the latitude-dependent temperature and salinity profiles we also use surface forcing values constant in latitude, longitude and time. Temperature and salinity values are set to 4°C and 34.8 in both models in order to generate circulations with homogeneous densities over the whole water column. The initial ocean values for temperature and salinity are set to 4°C and 34.8, respectively. In all experiments (OGCM and zonally averaged model) a restoring time constant of 30 d is used for both surface temperature and salinity.

Starting from rest both oceanic models are first integrated with restoring boundary conditions (Haney, 1971). After 2000 yr (3-D model), or 4000 yr (2-D model) we switch to mixed boundary conditions. After further 4000 yr (3-D model) or 1000 yr (2-D model) of integration both models have reached quasi equilibrium. The longer integration time needed for the OGCM equilibrium is due to the fact that after the switch to mixed boundary conditions deep water formation ceases in the north, while it increases at high southern latitudes. In order to achieve a circulation with northern sinking, a short freshwater perturbation was introduced at 75°S. This procedure allows the northern deep water formation to resume after the initial decrease.

Figure 1 depicts the meridional overturning obtained at the end of the spinup with non-constant restoring temperature and salinity profiles for OGCM (upper panel) and the zonally averaged model (lower panel) For the zonally averaged model the circulation is achieved with the closure scheme of WVH95. Using the WS91 scheme yields a similar circulation which is not shown here. The equilibrium circulations in the two models are similar with northern overturning cells reaching down to the ocean bottom. With a deep water formation rate of 24 Sv (1 Sv = 10^{-6} m^3 s^{-1}) the thermohaline circulation in the 3-D model is more vigorous than in the 2-D model, where northern sinking is only 16 Sv. The maximum values of the overturning cells are reached at a depth of 1500 m in the 3-D model and at 1000 m in the zonally averaged model. A clear difference between both models is the more pronounced Deacon cell in the ACC region of the 2-D model.

3. Experiments

Starting from the spinup circulations we introduced freshwater perturbations. The discharges are rectangular in time with a duration of two months and a strength of -20 m/yr. This corresponds to a discharge rate of 0.8 Sv. A southern location was chosen in order to determine a time lag between the onset of the perturbation and changes of the deep water formation in the northern hemisphere. In order to avoid a strong dilution of the discharge signal by the ACC the perturbation was applied at the northern border of the ACC channel (47.5°S). The duration of the discharge is shorter than the time needed by the fastest signals occurring in the OGCM (internal Kelvin waves, Kawase, 1987) or in the zonally averaged model to propagate from southern to northern mid-latitudes. The large amplitude of the perturbation is chosen in order to more easily identify changes in response to the freshwater flux.

To distinguish advective and diffusive mechanisms from baroclinic processes a passive color tracer is discharged at the same time and location. For experiments performed with the zonally averaged model we either use the closure scheme proposed in WVH95 or the original one described in WS91. Table 1 gives an overview of the experiments discussed here.

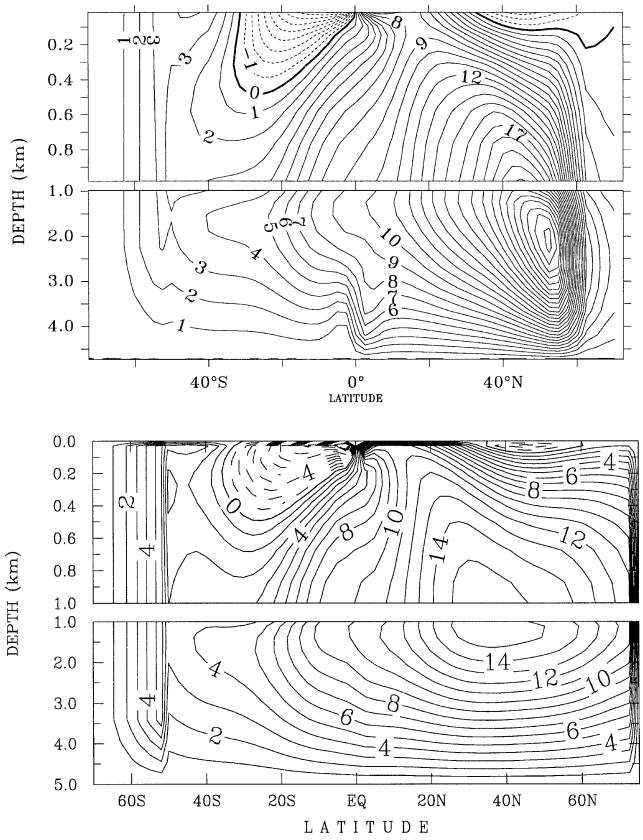

Fig. 1. Meridional overturning in Sv at the end of the spinup for the three-dimensional model (upper panel) and for the zonally averaged model (lower panel) run with the closure of WVH95.

Table 1. *Summary of experiments*

Experiment	Model	Stratification	Closure scheme
3D1	GFDL	yes	—
3D2	GFDL	no	—
WS1	WS91	yes	WS91
WS2	WS91	no	WS91
WVH1	WS91	yes	WVH95
WVH2	WS91	no	WVH95

In both models the freshwater perturbation is applied at 47.5°S. The discharges have durations of two months with an amplitude of $-20\,\mathrm{m\,yr^{-1}}$. WS91 and WVH95 denote closures schemes described in Wright and Stocker (1991) and Wright et al. (1995), respectively.

3.1. Propagation of density and color tracer

In this section we compare propagation patterns of density and color tracer anomalies simulated by the OGCM and the zonally averaged model. Results are summarized in Fig. 2, where baroclinic processes are visualized with Hovmoeller plots for temporal derivatives $\partial\rho/\partial t$ of sea water density (shading) and $\mathrm{d}C/\mathrm{d}t$ of the color tracer (contours). Using temporal derivatives rather than the anomalies lead to clearer pictures without distorting the progression speed. Results of the 3-D model obtained in experiments 3D1 and 3D2 are depicted in the uppermost panels. In the four lower panels we show propagation patterns simulated in the 2-D model in experiments WVH1, WVH2 (medium panels) and WS1, WS2 (bottom panels).

For experiments in the left panels the ocean is stratified; temperature and salinity are uniform before the onset of the freshwater discharge in the simulations shown on the right. In all panels the values are vertical averages over the uppermost 8 oceanic layers (0–500 m). Note that different time intervals are shown for experiments 3D1 and 3D2 (4 yr) than for experiments WVH1, WVH2, WS1 and WS2 (30 yr).

In the case of vertical stratification the most striking features common to experiments 3D1, WVH1 and WS1 are the different propagation patterns for $\partial\rho/\partial t$ and for $\mathrm{d}C/\mathrm{d}t$. While density signals rapidly reach the mid latitudes of the opposite hemisphere, the northward propagation of the color tracer is much slower. In experiment 3D1 a sharp density signal follows the characteristic path of an internal oceanic Kelvin wave (Kawase, 1987) and reaches the mid-latitudes of the northern hemisphere within 2 yr. The panels 'West', 'Equator' and 'East' denote sections of the Kelvin wave path from southern to northern mid-latitudes. Section 'West' is located at the western boundary and reaches from 75°S to the equator and values of $\mathrm{d}\rho/\mathrm{d}t$ are integrated over a zonal width of 7.5°. Similarly, section 'East' is located at the eastern basin boundary and extends from the equator to 75°N. Section 'Equator' covers the zonal basin width and $\mathrm{d}\rho/\mathrm{d}t$ is integrated from 3.75°S to 3.75°N.

In the zonally averaged model the density signal is more blurred, and reaches the opposite hemisphere after about 5–10 yr. There is a difference between experiment WVH1, where it is hardly possible to associate a northward propagation velocity with the density signal and experiment WS1, where a clear propagation velocity can be found. In experiment WVH1 density anomalies are simulated at the equator quasi-instantaneously after the onset of the freshwater discharge in the southern hemisphere. From the equator the density anomaly spreads northward and southward. At about 20°S the southern branch joins the northward moving anomaly related to advection and diffusion. The differences between the simulations WVH1 and WS1 will be further discussed in Section 3.2.

For a homogeneous ocean no difference can be seen between the progression of density anomalies and of the color tracer. In experiment 3D2 no internal Kelvin wave can build up, since the Brunt–Väisälä frequency is zero everywhere. As for the stratified cases the density and color tracer signals are much broader in the zonally averaged model than in the GFDL model.

Figure 3 depicts the evolution of the temporal derivative $\mathrm{d}\Psi_\mathrm{m}/\mathrm{d}t$ of the maximum northern meridional overturning cell. According to Fig. 2 the upper panel shows results from experiment 3D1, whereas the medium and bottom panels show $\mathrm{d}\Psi_\mathrm{m}/\mathrm{d}t$ for experiments WVH1 and WS1, respectively. Two vertical dashed lines mark the onset and the end of the freshwater discharge. In the OGCM $\mathrm{d}\Psi_\mathrm{m}/\mathrm{d}t$ reaches its maximum about 2 yr after the perturbation onset. This corresponds to the time needed for the internal Kelvin wave front to progress from southern mid-latitudes to northern mid-latitudes in the coarse resolution model. In the zonally averaged model the response of the northern overturning cell strongly depends on the choice of the used closure scheme. Using the WVH95 scheme (experiment WVH1, medium panel) yields a nearly instantaneous far-field response and maximum values of $\mathrm{d}\Psi_\mathrm{m}/\mathrm{d}t$ are reached after 1 yr. As in the 3-D model the sharp increase of $\mathrm{d}\Psi_\mathrm{m}/\mathrm{d}t$ is followed by a slower decrease. In experiment WS1 using the original closure scheme of WS91 leads to a much slower and smoother response of the ocean circulation. Here the maximum rate of change of the northern overturning cell is reached after 7–8 yr. Compared with the 3-D model, where maximum overturning change rates of $0.01\ \mathrm{Sv\ yr^{-1}}$ are reached, the response of the zonally averaged model is weaker for experiments WVH1 and WS1 with values of 0.006 and $0.002\ \mathrm{Sv\ yr^{-1}}$, respectively.

3.2. *Influence of the closure scheme in the zonally averaged model*

In a next step we investigate the differences between experiments WVH1 and WS1 due to the closure schemes for meridional velocities and meridional overturning, respectively.

On short time scales using eq. (1) as closure only leads to an initial response of the meridional velocity v. localized to the discharge area, where the density gradient has changed. On the other hand the meridional integration in eq. (2) allows for non-local responses. The third term on the right side of eq. (2) arises from meridional integration of the vertical vorticity component, zonally

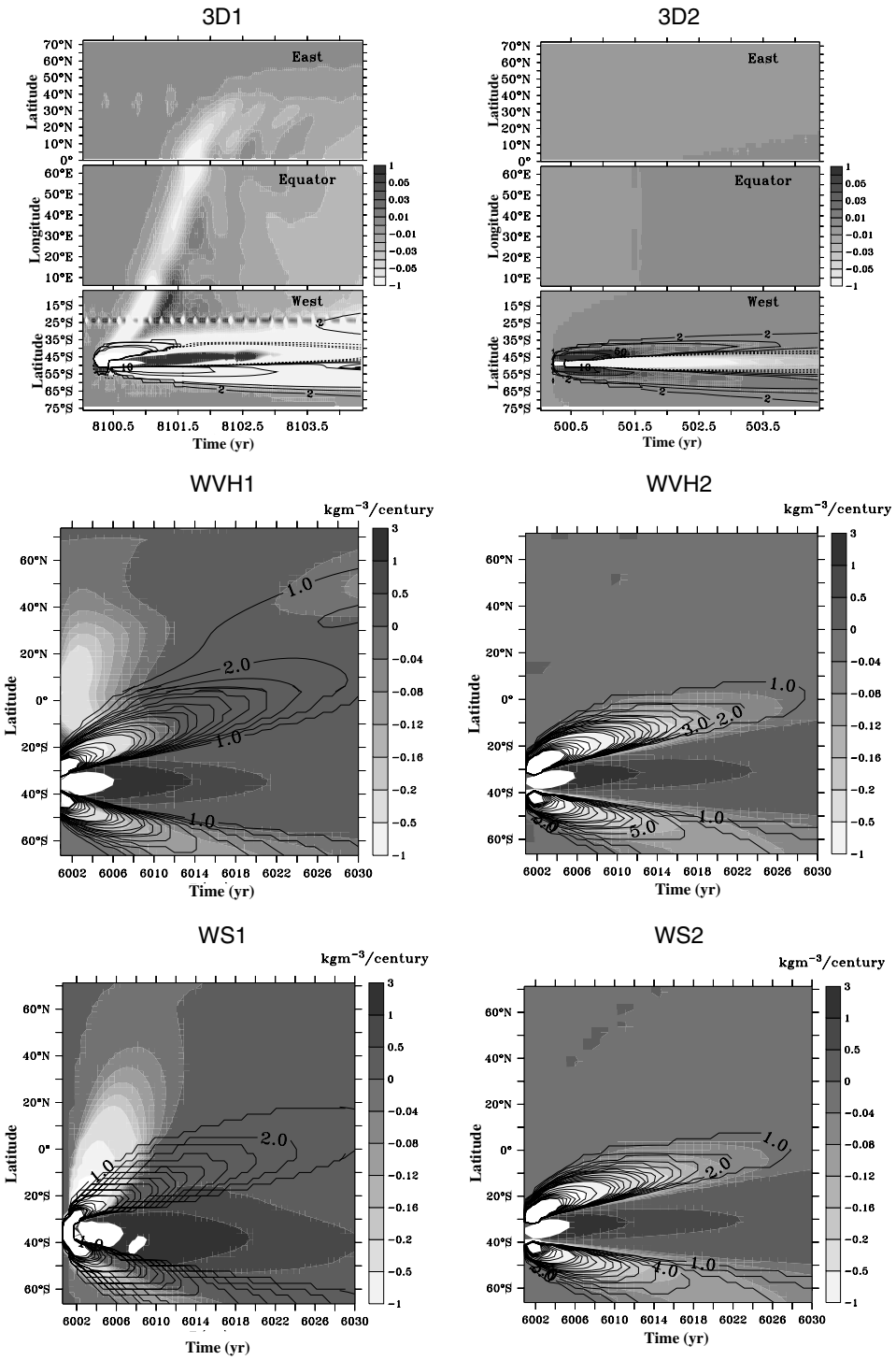
3D1
3D2
East
Equator
West
Latitude
Longitude
Time (yr)
WVH1
WVH2
WS1
WS2
kgm^{-3}/century
1.0
2.0
3.0
5.0

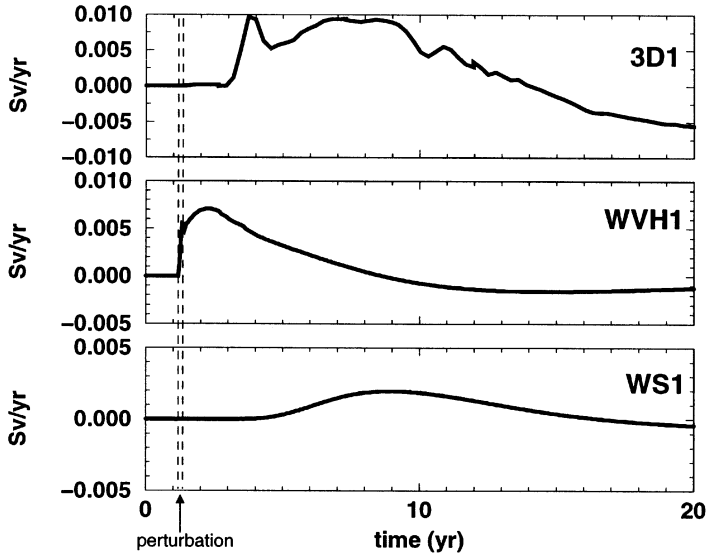

Fig. 3. Evolution of the temporal derivative of northern deep-water formation rates during and after freshwater discharges applied at 47.5°S for the OGCM (experiment 3D1, top panel) and for the zonally averaged model (experiments WVH1 and WS1, medium and bottom panels). The duration of the perturbation (between dashed lines) is two months in all experiments.

averaged across a western boundary layer (Wright et al., 1998). This term implies that a perturbation applied at high northern or southern latitudes is instantaneously felt at the equator. From there anomalies are generated poleward in both hemispheres due to the difference $\sigma - \sigma_{eq}$ in the first term of eq. (2). This term arises from the vorticity equation, zonally averaged over an inviscid basin interior and then integrated meridionally between the equator and an arbitrary latitude y.

The local and non-local characters of both closure schemes are illustrated in Figs. 4 and 5. Anomalies of the meridional and vertical velocities v, w in the surface layer (upper panels) and of $d\rho/dt$ (lower panels) are shown at the first (left panels) and second (right panels) integration time steps after the onset of the freshwater discharge. For both closure schemes we first observe density changes confined to the discharge area whereas surface velocity anomalies are zero everywhere (left panels of Figs. 4 and 5). At the next time step differences occur between the WVH95 and WS91 schemes. Using the WVH95 scheme leads to velocity anomalies reaching from the discharge area to the equator (left upper panel of Fig. 4). The same picture holds true for density anomalies which show changes over the same meridional extent. For the WS91 scheme velocity and density anomalies simulated at the second time step are confined to the discharge areas whereas the anomaly has a more pronounced amplitude than for the WVH95 scheme.

Fig. 2. Hovmoeller plots showing the propagation of temporal derivatives of density (shading) and of the color tracer (contour lines). The evolution is shown for the GFDL model (experiments 3D1, 3D2; uppermost panels) and for the zonally averaged model with the WVH95 and WS91 closures schemes for meridional velocities (experiments WVH1, WVH2, WS1 and WS2; medium and bottom panels). For experiments 3D1 and 3D2 the panels 'West', 'Equator' and 'East' denote sections of the Kelvin wave path from southern to northern mid-latitudes (see main text). In the simulations depicted in the left column the water is stratified according to the forcing profiles of temperature and salinity, whereas no density stratification is present in the experiments shown in the right. For all panels units are $kg\,m^{-3}$ $century^{-1}$. Note that time intervals shown for the zonally averaged model cover 30 yr, whereas an interval of 4 yr is depicted for the OGCM.

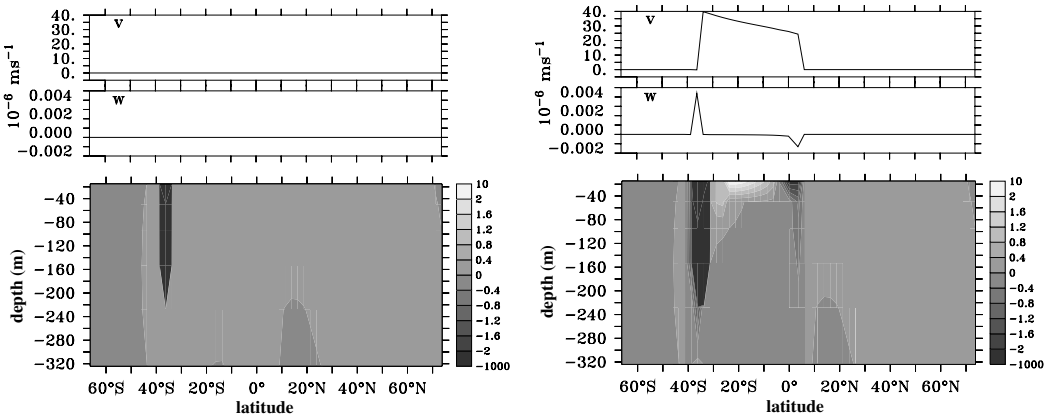

Fig. 4. Anomalies of the meridional and vertical velocity components (upper panels) and $d\rho/dt$ (lower panel) in the zonally averaged model. Units of $d\rho/dt$ are kg m^{-3} century^{-1}. The anomalies are shown at the first time step after the onset of the freshwater perturbation (left panels) and on the next time step (right panels). The calculation of the meridional velocity components is based on the WVH95 closure scheme.

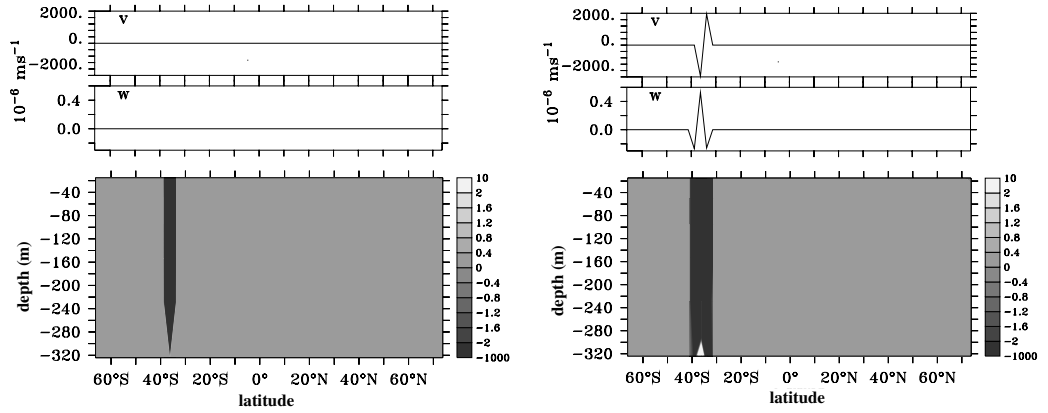

Fig. 5. Anomalies of the meridional and vertical velocity components (upper panels) and $d\rho/dt$ (lower panel) in the zonally averaged model. Anomalies are shown at the first time step after the onset of the freshwater perturbation (left panels) and on the next time step (right panels). The calculation of the meridional velocity components is based on the WS91 closure scheme. Units for $d\rho/dt$ are kg m^{-3} century^{-1}.

4. A conceptual box model for tracer propagation

The most obvious feature common to the 3-D and the 2-D models are the different propagation patterns observed for density and color tracer. In the 3-D model this is expected, since acceleration terms are retained in the momentum equations. Due to this more complete formulation of the momentum balance, internal waves can be generated in the OGCM. Since these waves are associated with vertical displacements of isopycnal surfaces their passage leads to density anomalies and to values $d\rho/dt \neq 0$ at a given depth. Typically the phase speed of internal waves is clearly faster than advection, and has values of about 3 m s^{-1} for the first baroclinic mode in the real ocean (Gill, 1982). In the zonally averaged model internal waves cannot be represented due to the absence of acceleration terms. However, even with this approximation, baroclinic processes allow density anomalies to propagate faster than color tracer anomalies.

In the following this feature will be addressed

with a conceptual box model. The motivation for using a box model, lies in its abitlity to represent in a simple manner all three approaches for calculating velocities discussed in the previous sections.

4.1. *Box model formulation*

The model consists of two superposed vertical layers of thicknesses Δz_1 and Δz_2 and horizontal length D, in which the exchange of two tracers C_1 and C_2 is achieved by advection only. The tracers C_1 and C_2 have different properties. Whereas C_2 is defined as a passive tracer, tracer C_1 affects the velocity field and therefore has properties similar to density. Each layer is divided up into 400 horizontal boxes of equal length. The box-model is illustrated in Fig. 6. The governing equations are the two-dimensional equations for advection,

$$\frac{\partial C_i}{\partial t} = -u\frac{\partial C_i}{\partial x} - w\frac{\partial C_i}{\partial z} \tag{3}$$

and for continuity

$$\frac{\partial u}{\partial x} + \frac{\partial w}{\partial z} = 0, \tag{4}$$

where u and w are the horizontal and vertical velocities, respectively. Three different approaches are assumed for the calculation of the horizontal velocity in the upper layer:

$$u(x) = u_0 + \alpha\frac{\partial C_1(x)}{\partial x}, \tag{5}$$

$$\begin{aligned} u(x) &= u_0 + \eta\int_0^x \frac{C_1(x)}{\partial x}\,\mathrm{d}x \\ &= u_0 + \eta[C_1(x) - C_1(0)], \end{aligned} \tag{6}$$

$$u(x) = u_0 + u'(x), \tag{7}$$

where

$$\frac{\partial u'(x)}{\partial t} = \frac{\partial u(x)}{\partial t} = \beta\frac{\partial C_1}{\partial x}$$

with constants $u_0 = 1$ (initial velocity), $\alpha = 1000$, $\eta = 0.1$ and $\beta = 0.6$. Using eq. (5), anomalies of $u(x)$ are determined by the horizontal gradient of C_1 ('density' tracer). This approach is similar to the original closure scheme for meridional velocities used in WS91. In eq. (6) the horizontal velocity depends on a horizontal integration of the gradient of C_1. This approach corresponds to a very simplified version of the WVH95 closure scheme. The difference on the right side of eq. (6) allows for a non-local response to localized perturbations. In eq. (7) we use the balance between the acceleration term and the horizontal gradient of C_1. This is similar to neglecting Coriolis, advective and friction terms in the momentum equation used in an OGCM and to replacing pressure by density and a vertical displacement of the ocean surface. The balance between acceleration term and horizontal pressure gradient still allows for gravity waves. Accordingly, the balance between acceleration and $\beta\,\partial C_1/\partial x$ ('pressure term') used in eq. (7) permits wave solutions in the box model.

4.2. *Experiments*

Whereas eqs. (5) and (6) are diagnostic, eq. (7) is prognostic. Using either eqs. (5), (6) or (7) we compare the propagation of the non-passive tracer C_1 with that of the passive tracer C_2. In the upper layer we impose the initial conditions for C_1 and C_2 shown in Fig. 6. In the lower layer we either set $C_1(x) = 1$ or $C_1(x) = 100$, whereas $C_2(x) = 1$ in all simulations.

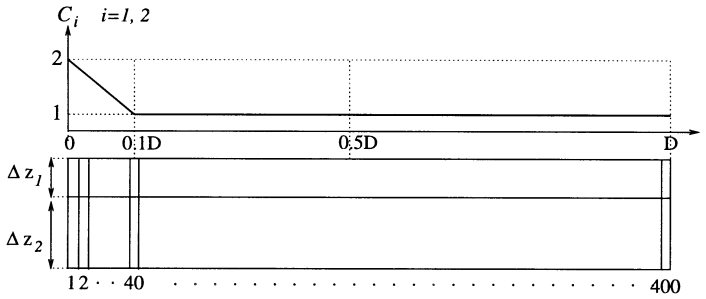

Fig. 6. Conceputal box-model consisting of two superposed layers of thickness Δz_1 and Δz_2. The horizontal model extent D is divided into 400 boxes. A triangular initial condition is chosen for C_i, $i = 1, 2$ in the upper layer. In the lower layer the initial value of C_1 is either set to 1 or 100, whereas C_2 is always set to 1.

Starting with these initial conditions the model is integrated forward in time (arbitrary time units). Figure 7 shows Hovmoeller plots for $\dot{C}_1$ and $\dot{C}_2$. Horizontal velocities are calculated according to eq. (7) (upper panels), eq. (6) (medium panels) and eq. (5) (lower panels). In the experiments shown in the left panels we set $C_1 = 100$ in the lower layer, whereas $C_1 = 1$ for the experiments shown on the right panels. As previously, shading indicates the temporal derivative $\dot{C}_1$ of the 'density' tracer, whereas the passive tracer $\dot{C}_2$ is represented with solid contours.

For the stratified cases anomalies of C_1 propagate clearly faster than those of C_2. This holds true for the three formulations of the horizontal velocity. The simulations based on eqs. (5) and (7) show distinct propagations of anomalies of C_1 along the horizontal domain, where the signal is more diffused if the horizontal velocity is based on eq. (5). If eq. (6) is used the simulation results in a qualitatively different propagation pattern. First anomaly signals occur at location $x = D$, from where they propagate back towards $x = 0$. This behavior is similar to experiment WVH1, where first anomalies are generated at the equator after a southern freshwater discharge. If $C_1 = 1$ in the lower layer at the beginning of the integration the propagation patterns of $\mathrm{d}\dot{C}_i$, $i = 1, 2$ are similar for the three cases. Anomalies of the non-passive tracer as well as of the passive tracer are entrained with velocity u_0.

The behaviour seen in Fig. 7 can be further elucidated by transforming the basic box-model equations. Based on eq. (5) the vertical velocity component w can be derived from eq. (4). Replacing u with eq. (5) in eq. (4) yields

$$\alpha \frac{\partial^2 C_1}{\partial x^2} = -\frac{\partial w}{\partial z}. \tag{8}$$

At the bottom of the upper layer with thickness Δz_1 the velocity component w can be calculated according to

$$\alpha \int_0^{\Delta z} = -\alpha \frac{\partial^2 C_1}{\partial x^2}\,\mathrm{d}z = -\int_0^{\Delta z} \frac{\partial w}{\partial z}\,\mathrm{d}z. \tag{9}$$

Since u is constant within one layer and $w(z) = 0$ for $z = 0$ the vertical component at the bottom of the first layer is given by

$$w(\Delta z) = -\alpha \frac{\partial^2 C_1}{\partial x^2}\,\Delta z_1. \tag{10}$$

The horizontal velocity u in the lower layer is calculated according to eq. (4), whereas $w = 0$ at the layer bottom.

Substituting eqs. (10) and (5) into eq. (3) for the upper layer yields

$$\frac{\partial C_i}{\partial t} = u_0 \frac{\partial C_i}{\partial x} + \alpha \frac{\partial C_1}{\partial x} \cdot \frac{\partial C_i}{\partial x} + \alpha \Delta z_1 \frac{\partial C_i}{\partial z} \cdot \frac{\partial^2 C_1}{\partial x^2}, \quad i = 1, 2. \tag{11}$$

The third term on the right side of eq. (11) has the form of a diffusion term with diffusion coefficients $\alpha \Delta z_1\ \partial C_i/\partial z$. For $C_1 = 100$ in the lower layer $|\partial C_1/\partial z| \geqslant |\partial C_2/\partial z|$. Since the surface initial conditions are similar for C_1 and C_2 the first two terms on the right side of eq. (11) ('classic advection' and non-linear term) are identical for both tracers at the first time step. The different evolutions of C_1 and C_2 arise because the absolute value of the diffusive term is higher for C_1 than for C_2. For an initial value $C_1 = 1$ in the lower layer the third term is identical for both tracers at the end of the first time step and subsequently $\partial C_1/\partial t = \partial C_2/\partial t$. Thus the values of C_1 and C_2 are identical for all following time steps and have the same long-term evolution.

Using eq. (6) for determining horizontal velocities leads to a progression velocity dependent on η and on the stratification $\Delta_z C_i = C_i(\text{bottom}) - C_i(\text{surface})$. Inserting eq. (6) into eq. (4) yields

$$\frac{\partial w}{\partial z} = -\eta \frac{\partial}{\partial x}[C_1(x) - C_1(0)], \tag{12}$$

$$w = -\eta \int_0^{\Delta z} \frac{\partial C_1}{\partial x}\,\mathrm{d}z = -\eta \Delta z \frac{\partial C_1}{\partial x}. \tag{13}$$

Fig. 7. Evolution of temporal derivatives $\dot{C}_1$ (shading) and $\dot{C}_2$ (contours). For experiments shown in the left panels $C_1 = 100$ in the lower layer (stratified), whereas right panels show the evolution for $C_1 = 1$ in the lower layer (not stratified). Velocity is either calculated according to eqs. (7) (uppermost panels), (6) (medium panels) and (5) (bottom panels).

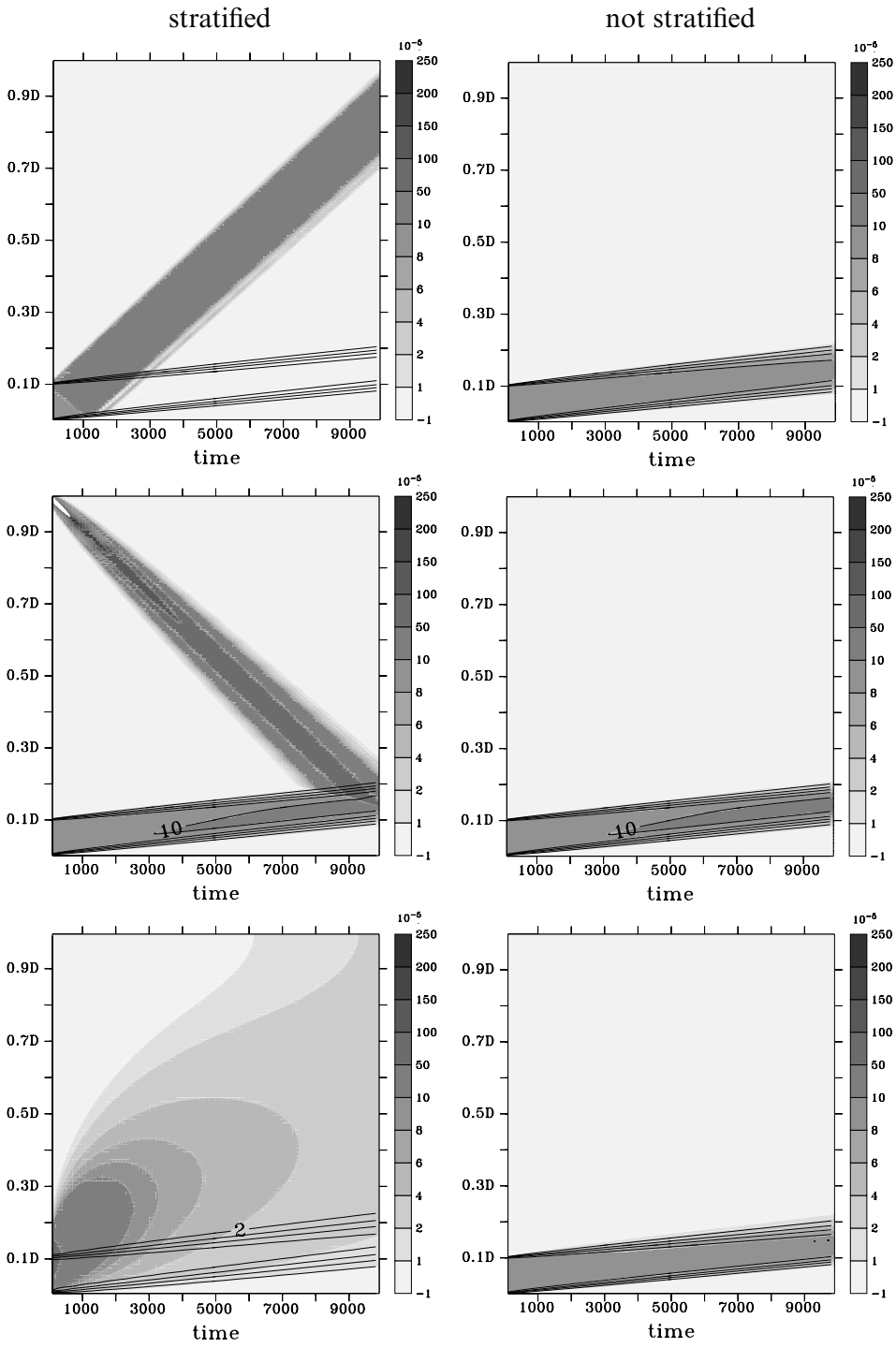
stratified
not stratified
0.9D
0.7D
0.5D
0.3D
0.1D
1000 3000 5000 7000 9000
time
10⁻⁵
250 200 150 100 50 10 8 6 4 2 1 −1
10
2

Substituting w in eq. (3) we obtain

$$\frac{\partial C_i}{\partial t} = -u\frac{\partial C_i}{\partial x} + \eta\Delta_z C_i \frac{\partial C_1}{\partial x}. \quad (14)$$

If we consider C_2, the difference $\Delta_z C_2$ is small and eq. (14) reduces to an advection equation with propagation speed u. For the non-passive tracer C_1 the difference $\Delta_z C_2 \gg \Delta_z C_2 \approx$ constant, and eq. (14) can be written as

$$\frac{\partial C_1}{\partial t} = -(u - \eta\Delta_z C_1)\frac{\partial C_1}{\partial x}. \quad (15)$$

The propagation speed $u - \eta\Delta_z C_1$ corresponds to the velocity of the backward propagating anomaly seen in Fig. 7. The upper panel of Fig. 8 shows a comparison of the backward propagation speed based on eq. (15) (dashed line) with those simulated in the box-model (thin solid line) for different stratifications of C_1 and two different values of η. The good agreement between both velocities suggests that the propagation speed of the backward branch is set up by the constant η and the stratification of C_1.

If the acceleration term is retained for the calculation of horizontal velocities [eq. (7)], we can derive a wave equation. Differentiating eq. (3) with respect to z yields

$$\frac{\partial^2 C_1}{\partial t\,\partial z} = -\frac{\partial u}{\partial z}\frac{\partial C_1}{\partial x} - u\frac{\partial^2 C_1}{\partial x\,\partial z} - \frac{\partial w}{\partial z}\frac{\partial C_1}{\partial z} - w\frac{\partial^2 C_1}{\partial z^2}. \quad (16)$$

For simplicity we consider cases where $u_0 = 0$. Plotting the left- and right-hand terms of eq. (1) indicates that the left term and the third term on the right side are dominant (not shown). Neglecting the other terms and making use of eq. (4) yields

$$\frac{\partial^2 C_1}{\partial t\,\partial z} = \frac{\partial u}{\partial x}\frac{\partial C_1}{\partial z}. \quad (17)$$

Differentiating eq. (7) with respect to x yields

$$\frac{\partial^3 C_1}{\partial x\,\partial z\,\partial t} = \frac{\partial^2 u}{\partial x^2}\frac{\partial C_1}{\partial z} + \frac{\partial u}{\partial x}\frac{\partial^2 C_1}{\partial x\,\partial z}. \quad (18)$$

A scale analysis shows that the second term on the right-hand side of eq. (18) is small compared to the other terms. Removing the second right-

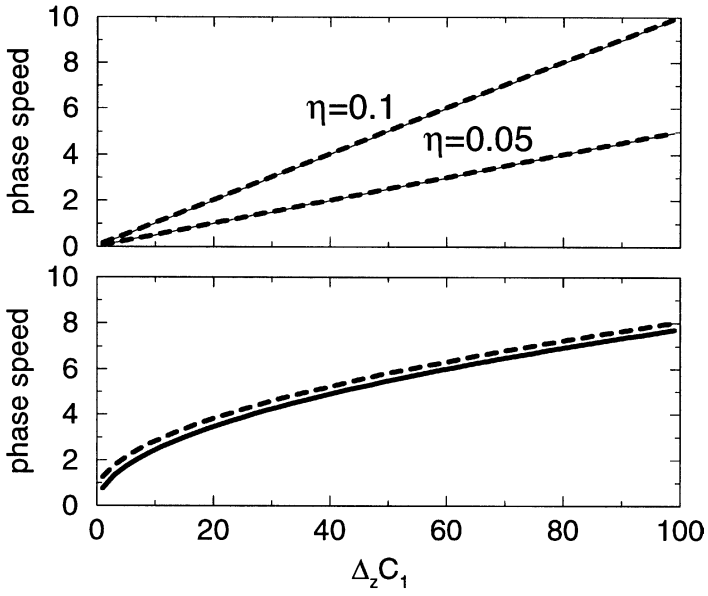

Fig. 8. Phase speeds (arbitrary units) associated with the propagation of anomalies of the tracer C_1 in dependence of the vertical stratification $\Delta_z C_1$. Upper panel: values simulated by using eq. (6) with $\eta = 0.1, 0.05$ in the box model (thin solid lines) and theoretical values based on eq. (15) (dashed lines). Lower panel: values simulated by using eq. (7) in the box model (solid line) compared to theoretical values based on eq. (20) (dashed line).

hand term and using $\partial^2(7)/\partial x\,\partial t$ yields

$$\frac{1}{\beta}\frac{\partial^3 u}{\partial z\,\partial t^2}=\frac{\partial^2 u}{\partial x^2}\frac{\partial C_1}{\partial z}. \tag{19}$$

Integrating eq. (19) with z leads to a wave equation

$$\frac{\partial^2 u}{\partial t^2}=\beta\Delta_z C_1\frac{\partial^2 u}{\partial x^2} \tag{20}$$

with phase velocity $c_{\mathrm{ph}}=\sqrt{\beta\Delta_z C_1}$ and $\Delta C_1=$ $C_1(\mathrm{bottom})-C_1(\mathrm{surface})$. The phase speed c_{ph} depends on the constant β as well as on the stratification of C_1. In the lower panel of Fig. 8 we compare phase speeds occurring in the box model with values obtained from eq. (20). The values simulated in the box model (solid line) are in good agreement with theoretical values c_{ph}. Since $\partial C_2/\partial z \ll \partial C_1/\partial z$ for the passive tracer C_2, eq. (3) nearly reduces to an advective equation without the vertical term. Anomalies of C_2 propagate with speed $u=u_0+u'$.

5. Conclusions and outlook

The present study showed that rapid changes of the large-scale oceanic circulation occur in models of different complexity. The propagation speed of density anomalies depends on the vertical density stratification (OGCM, zonally averaged model) and on the closure scheme used in the momentum eqs. (zonally averaged model). Besides the dimension one major difference between both oceanic models consists in the formulation of the momentum equations where acceleration and advection terms are neglected in the zonally averaged model, whereas they are retained in the OGCM.

The fastest density anomaly signals simulated by the OGCM are mediated by internal Kelvin waves. For perturbations applied at the northern border of the ACC the wave signal takes between 2 and 3 yr to reach the mid-latitudes of the northern hemisphere. In the zonally averaged model internal gravity waves are not represented, because acceleration terms are removed in the momentum equations. Nevertheless, a vertical density gradient causes a distinction in propagation speeds: density anomalies propagate faster than a color tracer being carried by advection/diffusion. The propagation speed of density anomalies depends on the choice of the closure scheme used in the momentum equations. Whereas density anomalies need about 10 yr for reaching the mid-latitudes of the northern hemisphere if the original WS91 scheme is used, the response is much faster for the WVH95 closure scheme. In this case, velocity and density anomalies reach the equator in one time step due to the non-local character of eq. (2). The zonally averaged vertical component of the vorticity equation is integrated between an arbitrary northern/southern latitude and the northern/southern limit of the ocean basin. This allows a quasi-instantaneous adjustment of the ocean circulation between the latitude of a freshwater discharge and the equator.

The fact that density anomalies propagate faster than advection of color tracer anomalies in both oceanic models is further elucidated with an advective box model including a density-like tracer C_1 and a passive tracer C_2. The horizontal velocity is based on representations according to eqs. (5), (6) and (7). Using the first approach which is similar to the WS91 closure leads to an additional diffusive term with a diffusion coefficient dependent on the vertical gradient of C_1 and C_2. Since $|\partial C_1/\partial z| > |\partial C_2/\partial z|$ this term is negligible for C_2. This leads to a faster propagation signal for C_1 than for C_2. Results based on eq. (6), which is similar to the WVH95 scheme, show a quasi-instantaneous far-field response for C_1, while C_2 progresses with advection speed only. If the acceleration term is retained for determining the horizontal velocity [similar to OGCM, eq. (7)], a wave equation can be derived for C_1 with phase speed dependent on the stratification of C_1.

The fast response occurring for density anomalies is also seen in the temporal evolution of the meridional overturning ψ_{m} during and after short freshwater pulses. For the closure of Wright et al. (1995) the response to a perturbation applied at the northern border of the ACC is quasi-instantaneous. A sharp increase of $\mathrm{d}\psi_{\mathrm{m}}/\mathrm{d}t$ is followed by a much slower gradual decrease. This is similar to the evolution simulated in the OGCM where a rapid increase of $\mathrm{d}\psi_{\mathrm{m}}/\mathrm{d}t$ coincides with the arrival of the internal Kelvin wave front. The main difference is given by the time lag between the onset of the freshwater discharge and the first changes of the northern deep-water formation cell, which only occurs after several years in the OGCM. If the WS91 closure is used the highest change rates of meridional overturning are reached after about 8 yr. In this case the fresh-

water discharge causes a slower and weaker increase and decrease of $d\psi_m/dt$.

Note that both closure schemes have shortcomings. Neither the slow response seen for the WS91 scheme nor the instantaneous changes due the WVH95 scheme represent the first adjustment phase of the oceanic circulation in a realistic way. However, as described in Wright et al. (1998), the instantaneous response seen for the WVH95 closure is justified by assuming a Munk boundary layer, which represents a steady-state solution where wave processes are already completed. If variability is considered on longer timescales (decadal upwards) the adjustment through wave processes can be considered as 'instantaneous' with respect to the time period of interest. Therefore, results based on the approach of WS95 are in closer agreement with the behavior of the OGCM which includes a more complete description of ocean dynamics. This result suggests that for the investigation of connections between the northern and southern hemispheres the WVH95 is superior to the earlier formulation of WS91.

6. Acknowledgement

This work was supported by the Swiss National Science Foundation and the European project 'Mileclim': Decadal and Centennial Climatic Variability during the Last Millenium in the North Atlantic and Europe'. Comments of three reviewers helped to improve this paper.

REFERENCES

Bender, M., Sowers, T., Dickson, M.-L., Orchardo, J., Grootes, P., Mayewski, P. A. and Meese, D. A. 1994. Climate correlations between Greenland and Antarctica during the past 100,000 years. *Nature* **372**, 663–666.

Blunier, T., Chappellaz, J., Schwander, J., Dällenbach, A., Stauffer, B., Stocker, T. F., Raynaud, D., Jouzel, J., Clausen, H. B., Hammer, C. U. and Johnsen, S. J. 1998. Asynchrony of Antarctic Greenland climate during the last glacial period. *Nature* **394**, 739–743.

Broecker, W. S. 1991. The great ocean conveyor. *Oceanography* **4**, 79–89.

Broecker, W. S. 1998. Paleocean circulation during the last deglaciation: a bipolar seesaw? *Paleoceanogr*. **13**, 119–121.

Bryan, K. 1969. A numerical method for the study of the circulation of the world ocean. *J. Comput. Phys.* **4**, 347–376.

Dickson, R. R. and Brown, J. 1994. The production of North Atlantic Deep Water: sources, rates, and pathways. *J. Geophys. Res.* **99**, 12,319–12,341.

Gill, A. E. 1982. *Atmosphere–ocean dynamics*. Volume 30 of *Int. Geophys. Ser*. Academic Press, San Diego, California, 662 pp.

Haney, R. L. 1971. Surface thermal boundary conditions for ocean general circulation models. *J. Phys. Oceanogr*. **1**, 241–248.

Hirschi, J., Sander, J. and Stocker, T. F. 1999. Intermittent convection, mixed boundary conditions and the stability of the thermohaline circulation. *Clin. Dynam.* **15**, 277–291.

Hsieh, W. W., Davey, M. K. and Wajsowicz, R. C. 1983. The free Kelvin wave in finite-difference numerical models. *J. Phys. Oceanogr*. **13**, 1383–1397.

Kawase, M. 1987. Establishment of deep ocean circulation driven by deep water production. *J. Phys. Oceanogr*. **17**, 2294–2317.

Latif, M., Roeckner, E., Mikolajewicz, U. and Voss, R. 2000. Tropical stabilization of the thermohaline circulation in a greenhouse warming simulation. *J. Clim.* **13**, 1′809–1813.

Maier-Reimer, E., Mikolajewicz, U. and Hasselmann, K. 1993. Mean circulation of the Hamburg LSG OGCM and its sensitivity to the thermohaline surface forcing. *J. Phys. Oceanogr*. **23**, 731–757.

Manabe, S. and Stouffer, R. J. 1997. Coupled ocean–atmosphere model response to freshwater input: comparisons to Younger Dryas event. *Paleoceanography* **12**, 321–336.

McDermott, D. A. 1996. The regulation of northern overturning by southern hemisphere winds. *J. Phys. Oceanogr*. **26**, 1234–1255.

Mikolajewicz, U. 1998. A meltwater-induced collapse of the 'conveyor belt' thermohaline circulation and its influence on the distribution of $\Delta^{14}C$ and $\delta^{18}O$ in the oceans. *J. Geophys. Res.* (in press).

Pacanowski, R. C. and Griffes, S. M. 2000. MOM 3.0 Manual ftp://ftp.gfdl.gov/pub/GFDL_MOM3/manual_3.ps.Z: GFDL. Technical Report.

Pierce, D. W., Barnett, T. P. and Mikokajewicz, U. 1995. Competing roles of heat and freshwater flux in forcing thermohaline oscillations. *J. Phys. Oceanogr*. **25**, 2046–2064.

Rahmstorf, S. 1996. Bifurcation of the Atlantic thermohaline circulation in response to changes in the hydrological cycle. *Nature* **378**, 145–149.

Schmitter, A., Appenzeller, C. and Stocker, T. F. 2000. Enhanced Atlantic freshwater export during El Niño. *J. Geophys. Res. Lett*. **27**, 1163–1166.

Stocker, T. F. 1998. The seesaw effect. *Science* **282**, 61–62.

Stocker, T. F. 2000. Past and future reorganizations in the climate system. *Q. Sci. Rev.* **19**, 301–319.

Stocker, T. F. and Wright, D.. G. 1991. Rapid transitions of the ocean's deep circulation induced by changes in surface water fluxes. *Nature* **351**, 729–732.

Toggweiler, J. and Samuels, B. 1993. Is the magnitude of the deep outflow from the Atlantic Ocean actually governed by southern hemisphere winds? In: *The global carbon cycle*, ed. M. Heimann, Vol. I15 of *NATO ASII*. Springer Verlag, Berlin, pp. 303–331.

Visbeck, M., Cullen, H., Krahmann, G. and Naik, N. 1998. An ocean model's response to North Atlantic Oscillation-like wind forcing. *Geophys. Res. Lett.* **25**, 4521–4524.

Weijer, W., de Ruijter, P. M., Dijkstra, H. A. and van Leeuwen, P. J. 1999. Impact of interbasis exchange on the Atlantic overturning circulation. *J. Phys. Oceanogr.* **29**, 2266–2284.

Wright, D. G. and Stocker, T. F. 1991. A zonally averaged ocean model for the thermohaline circulation. Part I: Model development and flow dynamics. *J. Phys. Oceanogr.* **21**, 1713–1724.

Wright, D. G., Stocker, T. F. and Mercer, D. 1998. Closures used in zonally averaged ocean models. *J. Phys. Oceanogr.* **28**, 791–804.

Wright, D. G., Vreugdenhil, C. B. and Hughes, T. M. 1995. Vorticity dynamics and zonally averaged ocean circulation models. *J. Phys. Oceanogr.* **25**, 2141–2154.